ODAM: GRADIENT-BASED INSTANCE-SPECIFIC VISUAL EXPLANATIONS FOR OBJECT DETECTION

Anonymous authors
Paper under double-blind review

ABSTRACT

We propose the gradient-weighted Object Detector Activation Maps (ODAM), a visualized explanation technique for interpreting the predictions of object detectors. Utilizing the gradients of detector targets flowing into the intermediate feature maps, ODAM produces heat maps that show the influence of regions on the detector's decision for each predicted attribute. Compared to previous works classification activation maps (CAM), ODAM generates instance-specific explanations rather than class-specific ones. We show that ODAM is applicable to both one-stage detectors and two-stage detectors with different types of detector backbones and heads, and produces higher-quality visual explanations than the state-of-the-art both effectively and efficiently. We next propose a training scheme, Odam-Train, to improve the explanation ability on object discrimination of the detector through encouraging consistency between explanations for detections on the same object, and distinct explanations for detections on different objects. Based on the heat maps produced by ODAM with Odam-Train, we propose Odam-NMS, which considers the information of the model's explanation for each prediction to distinguish the duplicate detected objects. We present a detailed analysis of the visualized explanations of detectors and carry out extensive experiments to validate the effectiveness of the proposed ODAM.

1 INTRODUCTION

Significant breakthroughs have been made in object detection and other computer vision tasks due to the development of deep neural networks (DNN) (Girshick et al., 2014b). However, the unintuitive and opaque process of DNNs makes them hard to interpret. As spatial convolution is a frequent component of state-of-the-art models for vision tasks, class-specific attention has emerged to interpret CNNs, which has been used to identify failure modes (Agrawal et al., 2016; Hoiem et al., 2012), debug models (Koh & Liang, 2017) and establish appropriate users' confidence about models (Selvaraju et al., 2017). These explanation approaches produce heat maps locating the regions in the input images that the model looked at, representing the influence of different pixels on the model's decision. Gradient visualization (Simonyan et al., 2013), Perturbation (Ribeiro et al., 2016), and Class Activation Map (CAM) (Zhou et al., 2016) are three widely adopted methods to generate the visual explanation map. However, these methods have primarily focused on image classification (Petsiuk et al., 2018; Fong & Vedaldi, 2017; Selvaraju et al., 2017; Chattopadhay et al., 2018; Wang et al., 2020b;a), or its variants, e.g., visual question answering (Park et al., 2018), video captioning (Ramanishka et al., 2017; Bargal et al., 2018), and video activity recognition (Bargal et al., 2018).

Generating explanation heat maps for object detectors is an under-explored area. The first work in this area is D-RISE (Petsiuk et al., 2021), which extends RISE (Petsiuk et al., 2018) for explaining image classifiers to object detectors. As a perturbation-based approach, D-RISE first randomly generates a large number of binary masks, resizes them to the image size, and then perturbs the original input to observe the change in the model's prediction. However, the large number of inference calculations makes the D-RISE computationally intensive, and the quality of the heat maps is influenced by the mask resolution (e.g., see Fig. 1b). Furthermore, D-RISE only generates an overall heat map for the predicted object, which is unable to show the influence of regions on the specific attributes of a prediction, e.g., class probability and regressed bounding box corner coordinates.

The popular CAM-based methods for image classification are not directly applicable to object detectors. CAM methods generate heat maps for classification via a linear combination of the weights and the activation maps, such as the popular Grad-CAM (Selvaraju et al., 2017) and its variants. However, Grad-CAM provides class-specific explanations, and thus produces heat maps that high-

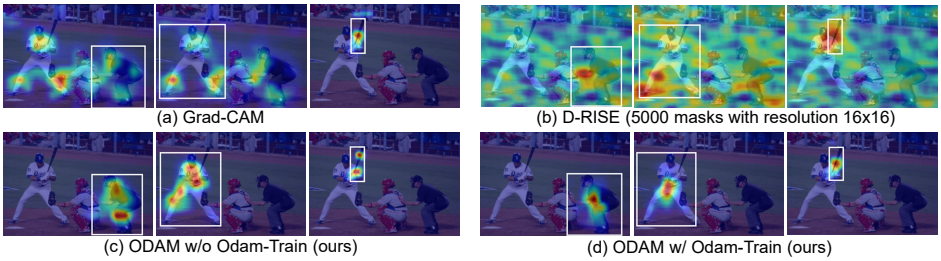

Figure 1: Comparison of heat maps from Grad-CAM (Selvaraju et al., 2017), D-RISE (Petsiuk et al., 2021) and our ODAM. The white box shows the corresponding detected object. (a) Grad-CAM highlights all objects of the same category (person) instead of the specific object instance. (b) D-RISE maps have noisy backgrounds and its effectiveness depends on the mask size; the 16x16 mask is better for smaller objects (baseball bat) than larger objects (person). (c) ODAM generates instance-specific heat maps with less noise and is robust to object size. (d) With Odam-Train, heat maps of each object are more compact, and separated from other objects.

light all objects of in a category instead of explaining a single detection (e.g., see Fig. 1a). For object detection, the explanations should be *instance-specific* rather than class-specific, so as to discriminate each individual object. Exploring the spatial importance of different objects can help interpret the models' decision and show the important area in the feature maps for each prediction.

Considering that direct application of existing CAM methods to object detectors is infeasible and the drawbacks of the current state-of-the-art D-RISE, we propose gradient-weighted *Object Detector Activation Maps* (ODAM). ODAM adopts a similar assumption as Grad-CAM that feature maps correlate with some concept for making the final outputs. Thus ODAM uses the gradients w.r.t. each pixel in the feature map to obtain the explanation heat map for each attribute of the object prediction. Compared with the perturbation-based D-RISE, ODAM is more efficient and generates less noisy heat maps (see Fig. 1c), while also explaining each attribute separately.

We also explore a unique explanation task for object detectors, *object discrimination*, which aims to indicate *which* object was detected. This is different from explaining the object class by visualizing the object parts. We propose a training scheme, Odam-Train, to improve the explanation ability for object discrimination by introducing both consistency and separation losses. The training encourages the model to produce consistent heat maps for the same object, and distinctive heat maps for different objects (see Fig. 1d). We further propose Odam-NMS, which uses the instance-level heat maps from ODAM and Odam-Train to aid the non-maximum suppression (NMS) process of removing duplicate predictions of the same object.

The contributions of our paper are summarized as follows:

1. We propose ODAM, a gradient-based visual explanation approach to produce instance-specific heat maps for explaining prediction attributes of object detectors, which is more efficient and robust compared with the current state-of-the-art.
2. We demonstrate the generalizability of ODAM by exhibiting explanations on both one-stage and two-stage detectors with different types of backbones and detector heads.
3. We explore a unique explanation task for detector, object discrimination, for showing which object was detected, and propose Odam-Train to improve object discrimination ability.
4. We propose Odam-NMS, which uses the instance-level heat maps generated by ODAM with Odam-Train to remove duplicate predictions during NMS, and its effectiveness verifies the object discrimination ability of ODAM with Odam-Train.

2 Related Works

Object detection Object detectors are generally composed of a backbone, neck and head. Based on the type of head, detectors can be mainly divided into one-stage and two-stage methods. Two-stage approaches perform two steps: generating region candidates (proposals) and then using RoI (Region of Interest) features for the subsequent object classification and location regression. The representative two-stage works are the R-CNN family, including R-CNN (Girshick et al., 2014a), Fast R-CNN (Girshick, 2015), Faster-RCNN (Ren et al., 2015), and Mask R-CNN (He et al., 2017). One-stage methods remove the RoI feature extraction and directly perform classification and regression on the entire feature map, and typical methods are YOLO (Redmon et al., 2016), RetinaNet (Lin et al., 2017b), and FCOS (Tian et al., 2019). Our ODAM can generate heat maps for both

one-stage and two-stage detectors with no limitation of the types of backbones and heads, and we adopt Faster R-CNN and FCOS in our experiments.

Explanation by visualization Since visualizing the importance of input features is a straightforward approach to interpret a model, many works visualize the internal representations of image classifier CNNs with heat maps. Gradient visualization methods (Simonyan et al., 2013) backpropagate the gradient of a target class score to the input image to highlight the "important" pixels, and other works (Springenberg et al., 2014; Zeiler & Fergus, 2014; Adebayo et al., 2018a) manipulate this gradient to improve the results qualitatively (see comparison in (Mahendran & Vedaldi, 2016)). The visualizations are fine-grained but not class-specific. Perturbation-based methods (Petsiuk et al., 2018; Ribeiro et al., 2016; Lundberg & Lee, 2017; Dabkowski & Gal, 2017; Chang et al., 2018; Fong & Vedaldi, 2017; Wagner et al., 2019) perturb the original input and observe the changes in output scores to determine the importance of regions. These black-box methods are intuitive and highly generalizable, but computationally intensive. Furthermore, the type or resolution of the perturbation greatly influences the quality of visualization results.

CAM-based explanations, e.g. CAM (Zhou et al., 2016), Grad-CAM (Selvaraju et al., 2017), and Grad-CAM++ (Chattopadhay et al., 2018), produce a heat map from a selected intermediate layer by linearly combining its feature activation maps with weights that indicate each feature's importance. For example, Grad-CAM defines the weights as the global average pooling of the corresponding gradient map, computed using back-propagation. Some gradient-free CAMs (Ramaswamy et al., 2020; Wang et al., 2020b;a) adopt the perturbation to generate weights from class score changes.

Although Grad-CAM has been adopted to study adversarial context patches in single-shot object detectors (Saha et al., 2020), the explanations are still category-specific. (Petsiuk et al., 2021) describes the reasons that make direct application of existing classifier explanation methods infeasible for object detector, and then proposes D-RISE based on RISE (Petsiuk et al., 2018), a black-box perturbation-based method. Hence, D-RISE inherits both the pros and cons of RISE, namely high-generalizability due to the black-box nature but time-consuming and noisy due to the inference procedure. Aiming to explore the possibility of white-box explanation of detectors, we propose ODAM, which utilizes gradient information to generate importance heat map for instance-specific detector explanations. Based on ODAM, we also propose Odam-Train training to improve the object discrimination of the instance-specific explanations, which is infeasible with the class-specific heat maps and the classification task.

Advanced NMS Classic NMS assumes that multiple instances rarely overlap, and thus high IoU (intersection over union) of two bounding boxes indicates duplicate detections. Several advanced NMS are proposed to mitigate the overdependence on IoU, e.g., SoftNMS (Bodla et al., 2017), AdaptiveNMS (Liu et al., 2019), Visibility Guided NMS (Gählert et al., 2020), and Relation Network Hu et al. (2018). These methods either use extra predicted cues, but still assume that high IoU correspond to duplicate detections, or modify the detectors to be more complex. Relying on IoU is not enough in crowded scenes where objects partially occlude each other, and thus their IoUs are naturally large. In these cases, internal information about the predictions is required. FeatureNMS Salscheider (2021) encodes feature embeddings for predictions and trains their distances between the same object to be smaller than those of different objects. In contrast, we propose Odam-NMS, which uses the correlations between instance-level heat maps together with IoUs to remove duplicate proposals of the same object. Compared with Salscheider (2021), our Odam-NMS is more stable and can also be interpreted to explain which objects were detected (i.e., object discrimination).

3 METHOD

We propose our ODAM for explaining object detection (Sec 3.1) with instance-level heat maps, Odam-Train (Sec. 3.2) for improving explanations for object discrimination, and Odam-NMS (Sec. 3.3) for NMS in crowd scenarios using these explanations.

3.1 ODAM: OBJECT DETECTOR ACTIVATION MAPS

Given an image $\mathcal{I}$, the detector model outputs multiple predictions, with each prediction p consisting of the class score $s_c^{(p)}$ and bounding box $B^{(p)} = (x_1^{(p)}, y_1^{(p)}, x_2^{(p)}, y_2^{(p)})$. Our goal is to generate heat maps to indicate the important regions that have a positive influence on the output of each prediction.

In Grad-CAM (Selvaraju et al., 2017) and its generalization Grad-CAM++ (Chattopadhay et al., 2018), the final score for a particular class Y_c is predicted from the whole image and the algorithm

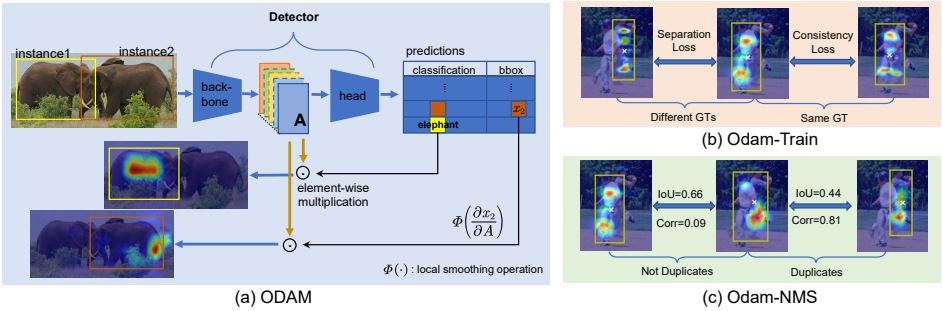

Figure 2: Our proposed framework. (a) Grad-ODAM generates instance-specific heat maps for explaining the predictions of an object detector; (b) ODAM-Train uses auxiliary losses to encourage heat maps for predictions on the same object to be consistent, and for different objects to be distinct; (c) ODAM-NMS uses the box IoU and the normalized correlation between heat maps to determine the duplicate detections. The bounding box shows the detection proposal corresponding to the heat map.

ignores distinguishing object instances within. Their explanation starts from the assumption that the score to be interpreted can be written as a linear combination of its global pooled last convolutional layer feature maps $\{A_k\}_k$, $Y_c = \sum_k w_k^c \sum_{ij} A_{ijk} = \sum_{ij} \sum_k w_k^c A_{ijk}$, where A_{ijk} indexes location (i, j) of A_k. Thus, the class-specific heat map $H_{ij}^c = \sum_k w_k^c A_{ijk}$ summarizes the feature maps with w_k^c capturing the importance of the k-th feature. To obtain the importance of each feature channel, Grad-CAM estimates w_k^c by global average pooling the gradient map $\partial Y_c / \partial A_k$, while Grad-CAM++ uses a weighted global pooling. However, both methods are limited to class-specific explanations, due to computing a channel-wise importance, which ignores the spatial discrimination information that is essential for interpreting different object instances.

Based on the above analysis, we assume that any predicted object attribute scalar $Y^{(p)}$ of a particular instance p can be written as a linear element-wise weighted combination of the feature map, and then the instance-specific heat map $H_{ij}^{(p)}$ can be produced by summarizing the feature maps with weight $w_{ijk}^{(p)}$ that captures the importance of *each pixel and each channel*,

$$Y^{(p)} = \sum\nolimits_k \sum\nolimits_{ij} w_{ijk}^{(p)} A_{ijk}, \quad H_{ij}^{(p)} = \sum\nolimits_k w_{ijk}^{(p)} A_{ijk}. \tag{1}$$

Previous gradient-based works (Simonyan et al., 2013; Springenberg et al., 2014; Selvaraju et al., 2017; Chattopadhay et al., 2018) have shown that the partial derivative w.r.t. A_{ijk} can reflect the influence of the k-th feature at (i, j) on the final output. However, such pixel-wise gradient maps are typically noisy, as visualized in (Simonyan et al., 2013). Thus, we set the importance weight map $w_k^{(p)}$ according to the gradient map $\partial Y^{(p)} / \partial A^k$ after a local smoothing operation Φ, and the corresponding heat map for scalar output $Y^{(p)}$ is obtained through a pixel-weighted mechanism:

$$w_k^{(p)} = \Phi\big(\tfrac{\partial Y^{(p)}}{\partial A^k}\big), \quad H^{(p)} = \mathrm{ReLU}\big(\sum\nolimits_k w_k^{(p)} \circ A^k\big), \tag{2}$$

where $\circ$ is element-wise multiplication. Here, local pooling is utilized on the gradient map to produce a smooth weight map, while maintaining the important spatial discrimination information. We adopt a Gaussian kernel for Φ in the experiments, and adaptively decide the size of the kernel based on the size of predicted object in the feature map.

When the scalar output $Y^{(p)}$ is a class score, ODAM highlights the important feature regions used by the detector to classify the instance p. Note that $Y^{(p)}$ could be any differentiable attribute of the predictions. For example, in our experiments we also examine the heat maps related to the predicted coordinates of the regressed bounding box (see Fig. 3). In addition to the fine-grained explanations for each predicted attribute, we also generate the heat map for the entire prediction by combining heat maps from classification and bounding box regression results using element-wise maximum, $H_{\text{comb}}^{(p)} = \max\{H_{\text{class}}^{(p)}, H_{\text{IoU}}^{(p)}\}$, where $H_{\text{class}}^{(p)}$ is the heat map for the predicted class, and $H_{\text{IoU}}^{(p)}$ is the heat map for the IoU (intersection over union) score between $B^{(p)}$ and the ground-truth box[1]

[1]If the ground-truth bounding box is not available, then the predicted value of $B^{(p)}$ can be used as a constant.

Our work is the first analysis and successful attempt to use the white-box method to generate instance-level explanations for object detector predictions, rather than only class-level explanations. With a PyTorch implementation, gradients of any scalar targets w.r.t. intermediate features can be calculated automatically Paszke et al. (2017). In this way, generating an ODAM explanation for one prediction takes about 2ms, which is much faster than the perturbation-based black-box method D-RISE, where using 5000 masks requires about 3 minutes to process one image with FCOS. In Sec. 4.1 and Sec.4.2, we qualitatively and quantitatively verify that the gradient-based method can effectively explain the predicted results for each detection proposal.

3.2 ODAM-TRAIN

Since the instance-specific heat maps may still "leak" onto other neighboring objects, especially in crowded scenes (e.g., see Fig. 4a), we propose a training method Odam-Train for improving the explanation ability of object discrimination to better show which object was being detected. In order to focus the detector to be more concentrated on a specific object area, and not overlapped with other objects, Odam-Train encourages similar attention for different predictions of the same object, and separate attentions for different objects. Specifically, we propose a heat-map consistency loss L_{con} and a separation loss L_{sep} as auxiliary losses during detector training. Heat maps are first calculated by ODAM for all the positive proposals, and then resized to the same size, and vectorized. The ODAM vectors are then organized by ground-truth object, where $\mathcal{P}^{(p)} = \{H_n^{(p)}\}_n$ is the set of ODAM vectors for positive predictions of the p-th ground-truth (GT) object. For each GT object, the best prediction $H_{\text{best}}^{(p)}$ is selected in $\mathcal{P}^{(p)}$ that has the highest IoU between its predicted bounding box and the GT box. Then, the *consistency and separation losses* are defined so that the ODAM vectors of the same object are consistent, while those of different objects are distinctive,

$$L_{\text{con}} = \sum_{p \in GT} \sum_{n \in \mathcal{P}^{(p)}} -\log \cos(H_{\text{best}}^{(p)}, H_n^{(p)}),\ L_{\text{sep}} = \sum_{p \in GT} \sum_{m \notin \mathcal{P}^{(p)}} -\log\left(1 - \cos(H_{\text{best}}^{(p)}, H_m^{(\neg p)})\right), \tag{3}$$

where $H_m^{(\neg p)}$ are ODAM vectors for proposals not corresponding to the n-th GT object. Finally, the auxiliary loss during detector training is: $L_{\text{aux}} = (L_{\text{con}} + L_{\text{sep}})/N$, where N is the total number of ODAM vector pairs during the loss calculation.

3.3 ODAM-NMS

In object detection, duplicated detections are removed in post-processing using NMS, which is based on the empirical assumption: two bounding boxes that are overlapped (high IoU) are likely to be duplicated, and the box with lower-score (less confidence) should be removed. In particular, for classical NMS, the predictions in list P are sorted by their confidence scores, then each prediction $p \in P$ is compared to the currently selected detections $d \in D$. If the IoU between p and any $d \in D$ is larger than a threshold T_{iou}, p is considered a duplicate and discarded. Otherwise p is added to D. The classical NMS has shortcomings in crowded scenes because the key assumption does not hold when objects are partially occluded by neighboring objects.

We propose Odam-NMS to mitigate this problem based on an observation that with Odam-Train, the ODAM heat maps for different objects can be distinctive, even though their bounding boxes are heavily overlapped (see the left and center heat maps in Fig. 2c). Meanwhile, even if the IoU of two predicted bounding boxes for the same object does not exceed the threshold, their explanation may be similar indicating the same object instance is detected. For example, in Fig. 2c, the center and right predictions have low box IoU (0.44) but have heat maps with high correlation (0.81). In other words, ODAM shows which object the model looked at to make the prediction, which can intuitively assist NMS to better identify duplicate object predictions.

In particular, after the inference stage of the detector, we use ODAM to generate heat maps for each prediction. All the heat maps are resized to the same size with a short edge length of 50, then vectorized. Normalized correlation is calculated between each pair of vectors to represent the probability that the two predictions correspond to the same object. Odam-NMS uses both the IoUs and heat map correlations between p and $d \in D$ when considering whether a prediction should be removed or kept. If the IoU is larger than T_{iou} while the correlation is very small ($corr \leq T^l$), then p is not a duplicate; On the contrary, if the IoU is small but the correlation is very near to one ($corr > T^h$), then p and the d are predicting the same object, which means p is a duplicate. Through these two conditions, Odam-NMS keeps more proposals in the high-IoU range for detecting highly-overlapped crowded objects, and removes more proposals in the low-IoU range for reducing duplicates. The pseudo code of Odam-NMS is in the Appendix.

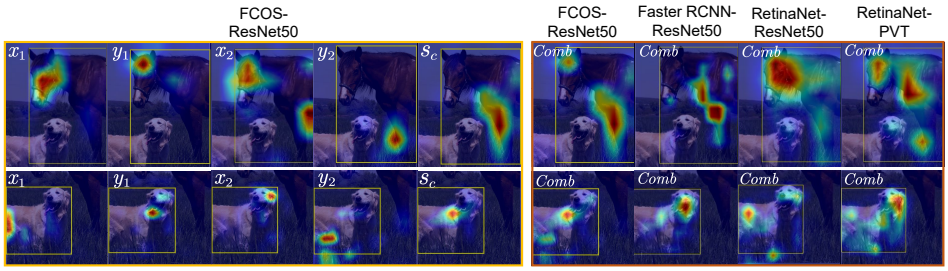

Figure 3: Heat map explanations of two instances (the horse and the dog) computed from different detectors with ResNet50 and pyramid vision transformer (PVT) as backbones. (left) The heat maps explain important regions for each predicted attribute (class score and the bbox coordinates) from FCOS. (right) The combined heat maps for the entire predictions for one-stage RetinaNet, FCOS and the two-stage Faster R-CNN.

4 EXPERIMENTS

In this section we conduct experiments on ODAM to: 1) evaluate its visual explanations qualitatively and quantitatively, and compare with the current state-of-the-art method D-RISE (Petsiuk et al., 2021); 2) evaluate the proposed Odam-NMS on crowded scenes. We mainly conduct the experiments with both one-stage detector FCOS (Tian et al., 2019) and two-stage detector Faster R-CNN, (Ren et al., 2015) using ResNet-50 (He et al., 2016) as the backbone and FPN (Lin et al., 2017a) as the neck. Two datasets are adopted for evaluation: MS COCO (Lin et al., 2014), a standard object detection dataset, and CrowdHuman (Shao et al., 2018), containing scenes with heavily overlapped objects. Experiments are performed using PyTorch and an RTX 3090 GPU. The training and testing hyperparameters are the same as those of the baseline detectors.

4.1 QUALITATIVE EVALUATION OF VISUAL EXPLANATIONS

Evaluation via visualization In order to verify the interpretability of visualizations, we generate visual explanations for different prediction targets (class score, bounding box regression values and their combination) of two specific instances using various detector architectures with the two types of backbones. Here we adopt the original baseline detector models (Odam-Train results are visualized in the next experiment). A set of example results are presented in Fig. 3, and we have the following observations from examining many such examples: 1) When predicting the object class, the model attends to the central areas of the object; 2) when regressing the bounding box, the model focuses on the extent of the object, while sometimes also looking at context information (e.g., for FCOS-ResNet50, the prediction of x_2 (right coordinate) of the horse uses its head on the left); 3) For the same target, models from different detectors show attention on different regions, even through they all detect the same instance with a high confidence. Thus, developers can have an intuitive judgment about the model through explanation maps. From the combination maps, which consider both classification and bounding box regression, the leg of the horse and the head of the dog are commonly important for the detectors, although the concrete heat maps look different.

Furthermore, we compare the instance-specific visualizations of Grad-CAM, D-RISE and our ODAM (w/o and w/ Odam-Train) in Fig. 1. The results are all generated with FCOS with FPN, and both Grad-CAM and ODAM use class score targets, while D-RISE uses the same mask settings as Petsiuk et al. (2021) to find the attention area of predictions. Our ODAM demonstrates a strong ability of generating clear and distinct instance-specific heat maps. In contrast, Grad-CAM is class-specific (highlighting all the people for each detected person), and D-RISE contains "speckles" in the background due to the random masking mechanism. See Appendix for more examples.

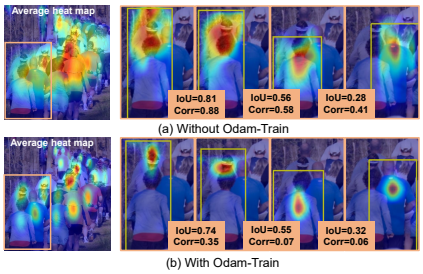

Figure 4: Comparison of heat maps from FCOS without and with Odam-Train. (left) The average heat map over the high-quality predictions with confidence score over 0.1. (right) Instance-specific heat maps of some predictions on different objects, with the IoU and correlation between each pair of predictions displayed in the middle.

Visualization w/ and w/o Odam-Train Next we compare the heat maps from ODAM using the baseline detector trained with and without Odam-Train. The heat maps for each proposal are computed by ODAM with their confidence score as the explanation targets. We find that although the original heat maps without Odam-Train (Fig. 4a) can locate the object well, the attention

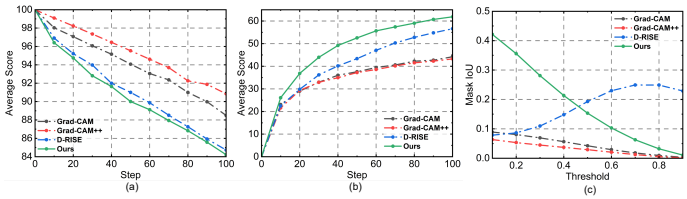

Figure 5: Average prediction score vs. (a) Deletion steps and (b) Insertion steps. (c) The pixel-level IoU between the ground truth object mask and explanation heatmap under different thresholds.

Table 1: Evaluation of faithfulness: AUC for Deletion, Insertion and Visual Explanation Accuracy (VEA) curves in Fig. 5.

Method	Del.↓	Ins.↑	VEA ↑
Grad-CAM	95.11	36.78	0.039
Grad-CAM++	96.57	36.18	0.027
D-RISE	92.11	43.35	0.157
ODAM	**91.50**	**50.33**	**0.163**

is spread to its overlapping neighbors, which makes the correlations between them relatively high. Using the consistency and separation losses in (3), Odam-Train yields concentrated heat maps for the same object and distinctive heat maps for different objects, which better shows which object was being detected, improving object discrimination. As seen in Fig. 4b, different people in the crowd can be separated by their low heat-map correlation, even when they have high IoU.

4.2 Quantitative evaluation of visual explanations

We evaluate faithfulness using Deletion, Insertion (Samek et al., 2016; Chattopadhay et al., 2018; Wang et al., 2020b;a; Petsiuk et al., 2021) and visual explanation accuracy (Oramas Mogrovejo et al., 2019), and also evaluate on the user trust of the produced visual explanations. For evaluating localization, we adopt Pointing games (Zhang et al., 2018). Meanwhile, we propose an object discrimination index (ODI) for measuring the interpretation ability of object discrimination. For comparison, we implement D-RISE using 5000 masks with resolution of 16×16 as in (Petsiuk et al., 2021). FCOS is used as baseline model and the features from FPN are adopted to generate heat maps. The best matched predictions of objects in the evaluation dataset are interpreted by each explanation method. Besides the MS COCO val set, results of the Pointing game and ODI are also reported on CrowdHuman validation sets.

Deletion and Insertion A faithful visual explanation map should highlight the important context on the image. Deletion replaces input image pixels by random values step-by-step using the ordering of the heatmap (most important first), then measures the amount of the prediction score drops (in percentage). Insertion is the reverse operation of deletion, and adds image pixels to an empty image in each step (based on heatmap importance) and records the average score increase. Since the sizes of objects vary a lot, we consider 1% of the bounding box area in each step and record results for 100 total steps. The average prediction scores on every 10 step are presented in Fig. 5(a-b), and Tab. 1 reports the area under the curve (AUC). Lower Deletion AUC means steeper drops in score, while higher Insertion AUC means larger increase in score with each step. Our methods have the fastest performance drop and largest performance increase for Deletion and Insertion, which shows that the regions highlighted in our heatmaps do have large effects on the detector predictions, as compared to other methods. Note that instance-specific explanations (ours and D-RISE) significantly surpass the classification explanation methods (Grad-CAM, Grad-CAM++).

Visual explanation accuracy The visual explanation accuracy (VEA) measures the pixel-level IoU between the ground-truth mask and the explanation heat map thresholded at different values. We use the MS COCO ground-truth object masks for this evaluation, and results are presented in Fig.5(c). Our method obtains the highest IoU when the threshold is small ($T < 0.4$), and the IoUs decrease as the threshold increases. This demonstrates that our heatmap energy is almost all inside the object (consistent with energy PG results in Tab. 4). In contrast, the low IoUs of the other three methods at a small threshold indicate that their heatmaps contains significant amounts of energy outside the object mask. For Grad-CAM/Grad-CAM++, the IoUs decrease when the threshold increases, which suggests that there are more large heat map values outside the object mask than inside the mask (they are not object-instance specific). For D-RISE, the IoU increases as the threshold increases, which indicates that the heat map values inside the object mask are larger than those outside the mask. Overall, our method has better IoU (0.421 at T=0.1) compared to D-RISE (0.249 at T=0.7), which is also verified by the AUC of the VEA curve in Tab. 1.

User Trust The interpretability of visual explanations is evaluated through a human trust test. Heat maps are generated by D-RISE, Grad-CAM, Grad-CAM++, and ODAM for 120 correctly-detected objects out of 80 classes from the MSCOCO val set (1-2 instances for each class). For each object, users are asked to rank the maps from the four methods by the order of which map gives

Table 2: User trust results: (left) percentage of rankings for each method; (right) average rank (AR).

Method	1st	2nd	3rd	4th	AR
Grad-CAM	3.9	12.9	30.5	52.7	3.3
Grad-CAM++	7.3	22.2	43.1	27.5	2.9
D-RISE	35.1	29.5	17.5	17.9	2.2
ODAM	**53.8**	35.4	8.9	1.9	**1.6**

Table 3: Comparison of Object Discrimination Index (%) on MSCOCO and CrowdHuman (CH), using either bounding box or mask ground-truth.

	MS COCO		CH
	box ↓	mask ↓	box ↓
Grad-CAM	77.0	72.7	91.4
Grad-CAM++	77.3	73.2	92.0
D-RISE	71.0	66.3	95.3
ODAM	*34.8*	*19.5*	*56.9*
w/ ODAM-Train	**34.1**	**18.7**	**51.3**

Table 4: Comparison of Pointing Game (PG) accuracy with ground-truth bounding boxes (b) or segmentation masks (m), energy-based PG with box or mask, and Heat Map Compactness (Comp.).

	MS COCO					CrowdHuman		
	PG(b)↑	PG(m)↑	enPG(b) ↑	enPG(m) ↑	Comp.↓	PG(b)↑	enPG(b) ↑	Comp.↑
Grad-CAM	26.7	22.5	20.7	15.0	4.34	15.7	9.7	3.99
Grad-CAM++	26.6	20.2	20.0	14.8	4.91	15.4	11.4	3.84
D-RISE	82.6	68.0	17.4	12.0	5.17	1.5	1.7	3.53
Ours	*91.9*	*82.6*	*73.1*	*57.1*	*1.36*	*95.5*	*79.5*	*1.04*
Ours w/ Odam-Train	**93.3**	**83.9**	**79.6**	**63.9**	**1.32**	**97.3**	**83.9**	**0.91**

more reasonable insight about how the target object was detected. We collect 10 responses for each object from a total number of 40 users (30 objects per user), totaling 1200 responses. The results are presented in Tab. 2. ODAM is ranked 1st place 53.8% of trials and 2nd place 35.4%, which is significantly better than D-RISE (χ^2 test, p<0.001). Overall, ODAM has significantly better average rank of 1.6 compared to others (Wilcoxon signed-rank test, p<0.001). The significantly higher human trust of ODAM demonstrate its superior instance-level interpretability for object detection.

From another aspect, previous studies evaluated trust between humans and machine learning systems by seeing if better models had better explanation maps according to humans. Following Selvaraju et al. (2017); Petsiuk et al. (2021), ODAM maps are generated for 120 objects that are correctly detected by two FCOS-ResNet50 models with different performance (36.6% mAP and 42.3% mAP). Excluding the samples where users thought the explanations were similar quality, the better model (42.3% mAP) received more responses (38.2% vs. 28.6%) that its explanations were more trustworthy. More details are provided in the Appendix.

Pointing Game To quantitatively evaluate the localization ability, we report results of the Pointing Game (PG) metric. In the PG, the maximum point in the instance-level heat map is extracted and a hit is scored if the point lies within the ground truth object region (either bounding box or segmentation mask). Then the PG accuracy is measured by averaging over the test objects. Since the PG only considers the maximum point, but not the spread of the heat map, we also adopt the energy-based PG (Wang et al., 2020b), which calculates the proportion of heat map energy within the GT object bounding box or segmentation mask (versus the whole map). Finally, to show the *compactness* of the heat map, we calculate the weighted standard deviation of heat-map pixels, relative to the maximum point: $Comp. = \left(\frac{1}{\sum_x S_x} \sum_x \frac{S_x ||x-\hat{x}||^2}{\frac{1}{4}(h^2+w^2)}\right)^{\frac{1}{2}}$, where S_x is the heat map value at location x, $\hat{x}$ is the maximum point of the heat map, and (w, h) are the width and height of the GT box. The denominator normalizes the distance w.r.t. the object size. Smaller compactness values indicate the heat map is more concentrated around the maximum point.

Both Grad-CAM and Grad-CAM++ perform poorly on both datasets since they generate class-specific heat maps. Our ODAM yields significant improvements over D-RISE on all the metrics. Specifically, D-RISE cannot work well on the CrowdHuman dataset, which only contains one object category. Since D-RISE uses the similarities between predictions of masked images and the original image to decide the mask weights, for datasets with few object categories, the predicted class probabilities provide less useful information when calculating the weights. Finally, using Odam-Train further improves the localization quality by generating more compact and well-localized heat maps.

Object Discrimination To evaluate the object discrimination ability of the heat maps, we propose the object discrimination index (ODI), which measures the amount of heat map energy that leaks to other objects. Specifically, for a given target object, the ODI is the proportion of heat map energy inside all other objects' bounding boxes (or segmentation masks) w.r.t. the total heat map energy inside all objects in the image (i.e., ignoring background regions). The averaged ODIs are presented

Table 5: Comparisons of different NMS strategies on the CrowdHuman validation set for both FCOS and Faster RCNN detectors. All the results are from models trained with the same baseline implementation.

	FCOS					Faster RCNN				
	AP↑	JI↑	MR↓	Recall	time (s/img)	AP↑	JI↑	MR↓	Recall	time (s/img)
NMS	87.8	78.4	45.5	93.2	0.114	86.9	79.5	43.2	90.3	0.092
Soft-NMS	80.8	74.9	89.0	93.0	0.47	76.5	61.9	84.8	92.3	0.284
FeatureNMS	89.3	78.1	45.6	95.4	0.145	82.0	65.7	68.8	**94.9**	0.120
Odam-NMS (ours)	**89.3**	**81.1**	**44.5**	**95.5**	0.178	**88.1**	**80.5**	**42.8**	91.5	0.140

in Tab. 3. Compared with others, ODAM consistently shows the least energy leaking out to other objects. Note that when using the tighter GT mask on MSCOCO, ODAM obtains the largest proportion of decrease, which indicates that the heat map can better focus on the explained target, even if its bounding box overlaps with other objects. Using Odam-Train significantly improves object discrimination in the crowded scenes of CrowdHuman.

4.3 Evaluating Odam-NMS

We evaluate Odam-NMS for improving detection in crowded scenes. We use ODAM with Odam-Train to generate explanation maps that have better object discrimination ability. To evaluate the performance of NMS on heavily overlapped situations, we adopt the CrowdHuman dataset (Shao et al., 2018), which contains an average 22.6 objects per image (2.4 overlapped objects). We compare Odam-NMS with NMS, SoftNMS, and FeatureNMS, using both FCOS and Faster RCNN. The IoU threshold is set to $T_{iou} = 0.5$ for both NMS and our method. Soft-NMS uses Gaussian decay with $\sigma = 0.5$ and final threshold of 0.05. For FeatureNMS, the IoU range is set to $(0.9, 0.1)$ following Salscheider (2021). The aspect ratios of the anchors in Faster R-CNN are set to $H : W = \{1, 2, 3\}$ based on the dataset, and other parameters are the same as in the baselines. Training runs for 30 epochs. We use $T^h = 0.8$, $T^l = 0.2$ based on the ablation study in the Appendix. We adopt three evaluation criteria: *Average Precision* (AP_{50}); *Log-Average Missing Rate* (MR), commonly used in pedestrian detection, which is sensitive to false positives (FPs); *Jaccard Index* (JI). See Chu et al. (2020) for details. Smaller MR indicates better results, while larger AP_{50} and JI are better.

Tab. 5 shows the results. Soft-NMS performs poorly in crowd scenes, generating many false positives in high-score region (high MR) with a long processing time. For FCOS, AP performance of FeatureNMS is much higher than NMS, while JI and MR are similar. However for Faster RCNN, although FeatureNMS obtains a high recall, the others are worse than NMS, indicating that the feature embeddings trained with the cropped features in two-stage detectors are not distinctive enough, and there are many false positives in detections. The learned embeddings in FeatureNMS have no explicit meaning except the relative distance between each pair, while Odam-NMS directly uses heat maps that offer explanations of the detector model. With the default IoU threshold, our Odam-NMS achieves better JI and MR than NMS and FeatureNMS for both detectors (FCOS and Faster RCNN). Meanwhile, Odam-NMS also achieves the best AP with Faster RCNN. The limitation of Odam-NMS is that generating heat maps for dense predictions costs a slightly longer processing time. Overall, these results verify the object discrimination interpretation ability of ODAM with Odam-Train and demonstrate that the instance-level explanation for predictions can help improve NMS in crowd scenes.

5 Conclusion

In this paper, we propose ODAM, a white-box gradient-based instance-level visualized explanation technique for interpreting the predictions of object detectors. ODAM can produce instance-specific heat maps for any prediction attribute, including object class and bounding box coordinates, to show the important regions that the model uses to make its prediction. Our method is general and applicable to both one-stage and two-stage detectors with different detector backbones, and heads. Qualitative and quantitative evaluations demonstrate the advantages of our method compared with the class-specific (Grad-CAM) or black-box works (D-RISE). We also propose a training scheme, OdamTrain, which trains the detector to produce more consistent explanations for the same detected object, and distinct explanations for different objects, thus improving object discrimination. Experiments show that Odam-Train is effective at improving localization in the explanation map and object discrimination. Finally, we propose Odam-NMS, which utilizes the explainability of ODAM to identify and remove duplicate predictions in crowd scenarios. Experiments on different detector architectures confirm its effectiveness, and further verify the interpretability provided by ODAM.

REFERENCES

Julius Adebayo, Justin Gilmer, Ian Goodfellow, and Been Kim. Local explanation methods for deep neural networks lack sensitivity to parameter values. *arXiv preprint arXiv:1810.03307*, 2018a.

Julius Adebayo, Justin Gilmer, Michael Muelly, Ian Goodfellow, Moritz Hardt, and Been Kim. Sanity checks for saliency maps. *Advances in neural information processing systems*, 31, 2018b.

Aishwarya Agrawal, Dhruv Batra, and Devi Parikh. Analyzing the behavior of visual question answering models. *arXiv preprint arXiv:1606.07356*, 2016.

Sarah Adel Bargal, Andrea Zunino, Donghyun Kim, Jianming Zhang, Vittorio Murino, and Stan Sclaroff. Excitation backprop for rnns. In *Proceedings of the IEEE Conference on Computer Vision and Pattern Recognition*, pp. 1440–1449, 2018.

Navaneeth Bodla, Bharat Singh, Rama Chellappa, and Larry S Davis. Soft-nms–improving object detection with one line of code. In *Proceedings of the IEEE international conference on computer vision*, pp. 5561–5569, 2017.

Chun-Hao Chang, Elliot Creager, Anna Goldenberg, and David Duvenaud. Explaining image classifiers by counterfactual generation. *arXiv preprint arXiv:1807.08024*, 2018.

Aditya Chattopadhay, Anirban Sarkar, Prantik Howlader, and Vineeth N Balasubramanian. Grad-cam++: Generalized gradient-based visual explanations for deep convolutional networks. In *2018 IEEE winter conference on applications of computer vision (WACV)*, pp. 839–847. IEEE, 2018.

Xuangeng Chu, Anlin Zheng, Xiangyu Zhang, and Jian Sun. Detection in crowded scenes: One proposal, multiple predictions. In *Proceedings of the IEEE/CVF Conference on Computer Vision and Pattern Recognition*, pp. 12214–12223, 2020.

Piotr Dabkowski and Yarin Gal. Real time image saliency for black box classifiers. *Advances in neural information processing systems*, 30, 2017.

Ruth C Fong and Andrea Vedaldi. Interpretable explanations of black boxes by meaningful perturbation. In *Proceedings of the IEEE international conference on computer vision*, pp. 3429–3437, 2017.

Nils Gählert, Niklas Hanselmann, Uwe Franke, and Joachim Denzler. Visibility guided nms: Efficient boosting of amodal object detection in crowded traffic scenes. *arXiv preprint arXiv:2006.08547*, 2020.

Ross Girshick. Fast r-cnn. In *Proceedings of the IEEE international conference on computer vision*, pp. 1440–1448, 2015.

Ross Girshick, Jeff Donahue, Trevor Darrell, and Jitendra Malik. Rich feature hierarchies for accurate object detection and semantic segmentation. In *Proceedings of the IEEE conference on computer vision and pattern recognition*, pp. 580–587, 2014a.

Ross Girshick, Jeff Donahue, Trevor Darrell, and Jitendra Malik. Rich feature hierarchies for accurate object detection and semantic segmentation. In *Proceedings of the IEEE conference on computer vision and pattern recognition*, pp. 580–587, 2014b.

Kaiming He, Xiangyu Zhang, Shaoqing Ren, and Jian Sun. Deep residual learning for image recognition. In *Proceedings of the IEEE conference on computer vision and pattern recognition*, pp. 770–778, 2016.

Kaiming He, Georgia Gkioxari, Piotr Dollár, and Ross Girshick. Mask r-cnn. In *Proceedings of the IEEE international conference on computer vision*, pp. 2961–2969, 2017.

Derek Hoiem, Yodsawalai Chodpathumwan, and Qieyun Dai. Diagnosing error in object detectors. In *European conference on computer vision*, pp. 340–353. Springer, 2012.

Han Hu, Jiayuan Gu, Zheng Zhang, Jifeng Dai, and Yichen Wei. Relation networks for object detection. In *Proceedings of the IEEE conference on computer vision and pattern recognition*, pp. 3588–3597, 2018.

Pang Wei Koh and Percy Liang. Understanding black-box predictions via influence functions. In *International conference on machine learning*, pp. 1885–1894. PMLR, 2017.

Tsung-Yi Lin, Michael Maire, Serge Belongie, James Hays, Pietro Perona, Deva Ramanan, Piotr Dollár, and C Lawrence Zitnick. Microsoft coco: Common objects in context. In *European conference on computer vision*, pp. 740–755. Springer, 2014.

Tsung-Yi Lin, Piotr Dollár, Ross Girshick, Kaiming He, Bharath Hariharan, and Serge Belongie. Feature pyramid networks for object detection. In *Proceedings of the IEEE conference on computer vision and pattern recognition*, pp. 2117–2125, 2017a.

Tsung-Yi Lin, Priya Goyal, Ross Girshick, Kaiming He, and Piotr Dollár. Focal loss for dense object detection. In *Proceedings of the IEEE international conference on computer vision*, pp. 2980–2988, 2017b.

Songtao Liu, Di Huang, and Yunhong Wang. Adaptive nms: Refining pedestrian detection in a crowd. In *Proceedings of the IEEE/CVF conference on computer vision and pattern recognition*, pp. 6459–6468, 2019.

Scott M Lundberg and Su-In Lee. A unified approach to interpreting model predictions. *Advances in neural information processing systems*, 30, 2017.

Aravindh Mahendran and Andrea Vedaldi. Salient deconvolutional networks. In *European conference on computer vision*, pp. 120–135. Springer, 2016.

José Antonio Oramas Mogrovejo, Kaili Wang, and Tinne Tuytelaars. Visual explanation by interpretation: Improving visual feedback capabilities of deep neural networks. In *https://iclr.cc/Conferences/2019/AcceptedPapersInitial*. openReview, 2019.

Dong Huk Park, Lisa Anne Hendricks, Zeynep Akata, Anna Rohrbach, Bernt Schiele, Trevor Darrell, and Marcus Rohrbach. Multimodal explanations: Justifying decisions and pointing to the evidence. In *Proceedings of the IEEE Conference on Computer Vision and Pattern Recognition*, pp. 8779–8788, 2018.

Adam Paszke, Sam Gross, Soumith Chintala, Gregory Chanan, Edward Yang, Zachary DeVito, Zeming Lin, Alban Desmaison, Luca Antiga, and Adam Lerer. Automatic differentiation in pytorch. 2017.

Vitali Petsiuk, Abir Das, and Kate Saenko. Rise: Randomized input sampling for explanation of black-box models. *arXiv preprint arXiv:1806.07421*, 2018.

Vitali Petsiuk, Rajiv Jain, Varun Manjunatha, Vlad I Morariu, Ashutosh Mehra, Vicente Ordonez, and Kate Saenko. Black-box explanation of object detectors via saliency maps. In *Proceedings of the IEEE/CVF Conference on Computer Vision and Pattern Recognition*, pp. 11443–11452, 2021.

Vasili Ramanishka, Abir Das, Jianming Zhang, and Kate Saenko. Top-down visual saliency guided by captions. In *Proceedings of the IEEE conference on computer vision and pattern recognition*, pp. 7206–7215, 2017.

Harish Guruprasad Ramaswamy et al. Ablation-cam: Visual explanations for deep convolutional network via gradient-free localization. In *Proceedings of the IEEE/CVF Winter Conference on Applications of Computer Vision*, pp. 983–991, 2020.

Joseph Redmon, Santosh Divvala, Ross Girshick, and Ali Farhadi. You only look once: Unified, real-time object detection. In *Proceedings of the IEEE conference on computer vision and pattern recognition*, pp. 779–788, 2016.

Shaoqing Ren, Kaiming He, Ross Girshick, and Jian Sun. Faster r-cnn: Towards real-time object detection with region proposal networks. *arXiv preprint arXiv:1506.01497*, 2015.

Marco Tulio Ribeiro, Sameer Singh, and Carlos Guestrin. " why should i trust you?" explaining the predictions of any classifier. In *Proceedings of the 22nd ACM SIGKDD international conference on knowledge discovery and data mining*, pp. 1135–1144, 2016.

Aniruddha Saha, Akshayvarun Subramanya, Koninika Patil, and Hamed Pirsiavash. Role of spatial context in adversarial robustness for object detection. In *Proceedings of the IEEE/CVF Conference on Computer Vision and Pattern Recognition Workshops*, pp. 784–785, 2020.

Niels Ole Salscheider. Featurenms: Non-maximum suppression by learning feature embeddings. In *2020 25th International Conference on Pattern Recognition (ICPR)*, pp. 7848–7854. IEEE, 2021.

Wojciech Samek, Alexander Binder, Grégoire Montavon, Sebastian Lapuschkin, and Klaus-Robert Müller. Evaluating the visualization of what a deep neural network has learned. *IEEE transactions on neural networks and learning systems*, 28(11):2660–2673, 2016.

Ramprasaath R Selvaraju, Michael Cogswell, Abhishek Das, Ramakrishna Vedantam, Devi Parikh, and Dhruv Batra. Grad-cam: Visual explanations from deep networks via gradient-based localization. In *Proceedings of the IEEE international conference on computer vision*, pp. 618–626, 2017.

Shuai Shao, Zijian Zhao, Boxun Li, Tete Xiao, Gang Yu, Xiangyu Zhang, and Jian Sun. Crowdhuman: A benchmark for detecting human in a crowd. *arXiv preprint arXiv:1805.00123*, 2018.

Karen Simonyan, Andrea Vedaldi, and Andrew Zisserman. Deep inside convolutional networks: Visualising image classification models and saliency maps. *arXiv preprint arXiv:1312.6034*, 2013.

Jost Tobias Springenberg, Alexey Dosovitskiy, Thomas Brox, and Martin Riedmiller. Striving for simplicity: The all convolutional net. *arXiv preprint arXiv:1412.6806*, 2014.

Zhi Tian, Chunhua Shen, Hao Chen, and Tong He. Fcos: Fully convolutional one-stage object detection. In *Proceedings of the IEEE/CVF International Conference on Computer Vision*, pp. 9627–9636, 2019.

Jorg Wagner, Jan Mathias Kohler, Tobias Gindele, Leon Hetzel, Jakob Thaddaus Wiedemer, and Sven Behnke. Interpretable and fine-grained visual explanations for convolutional neural networks. In *Proceedings of the IEEE/CVF Conference on Computer Vision and Pattern Recognition*, pp. 9097–9107, 2019.

Haofan Wang, Rakshit Naidu, Joy Michael, and Soumya Snigdha Kundu. Ss-cam: Smoothed score-cam for sharper visual feature localization. *arXiv preprint arXiv:2006.14255*, 2020a.

Haofan Wang, Zifan Wang, Mengnan Du, Fan Yang, Zijian Zhang, Sirui Ding, Piotr Mardziel, and Xia Hu. Score-cam: Score-weighted visual explanations for convolutional neural networks. In *Proceedings of the IEEE/CVF conference on computer vision and pattern recognition workshops*, pp. 24–25, 2020b.

Matthew D Zeiler and Rob Fergus. Visualizing and understanding convolutional networks. In *European conference on computer vision*, pp. 818–833. Springer, 2014.

Jianming Zhang, Sarah Adel Bargal, Zhe Lin, Jonathan Brandt, Xiaohui Shen, and Stan Sclaroff. Top-down neural attention by excitation backprop. *International Journal of Computer Vision*, 126 (10):1084–1102, 2018.

Bolei Zhou, Aditya Khosla, Agata Lapedriza, Aude Oliva, and Antonio Torralba. Learning deep features for discriminative localization. In *Proceedings of the IEEE conference on computer vision and pattern recognition*, pp. 2921–2929, 2016.

A Appendix

A.1 Odam-NMS

The pseudo-code for Odam-NMS is presented in Algorithm 1.

A.2 User trust test

We present the form of the questionnares and some samples that we used in the two user trust tests in Fig. 6.

Algorithm 1 Odam-NMS: predictions are removed or kept based on both the IoU and the correlation between ODAM heat maps.

$P \leftarrow GetPredictions(imageI)$
$P \leftarrow SORT(P)$
$D \leftarrow \emptyset$
while $P \neq \emptyset$ **do**
  $p \leftarrow POP(P)$
  $isDuplicate \leftarrow false$
  for $d \in D$ **do**
    $iou \leftarrow GetIoU(p, d)$
    $corr \leftarrow NormCorrelation(S_{yc}^{(p)}, S_{yc}^{(d)})$
    if $iou \geq T_{iou}$ **and** $corr > T^l$ **then**
      $isDuplicate \leftarrow true$
    else if $iou < T_{iou}$ **and** $corr > T^h$ **then**
      $isDuplicate \leftarrow true$
    end if
  end for
  if $\neg isDuplicate$ **then**
    $PUSH(p, D)$
  end if
end while

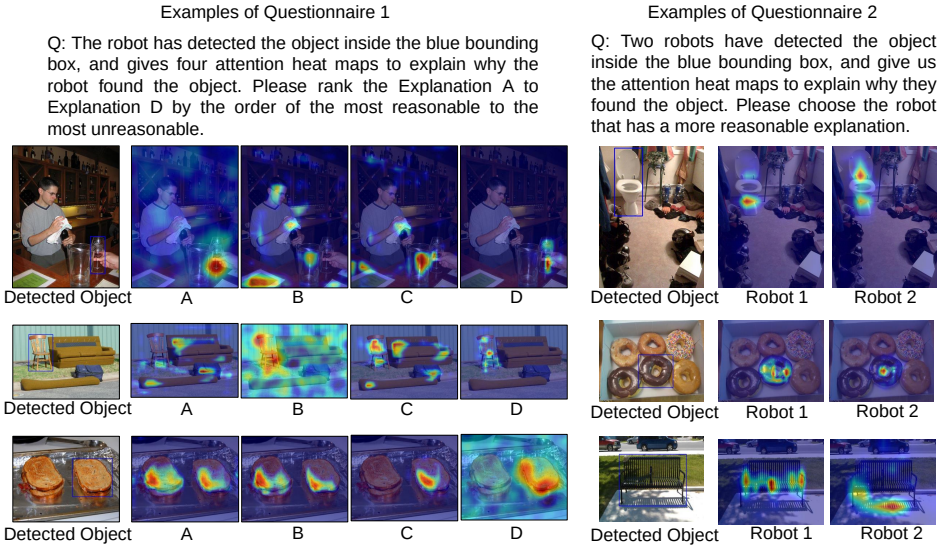

Figure 6: In the first questionnaire, the human needs to rank the heat maps from four explanation methods, including D-RISE, Grad-CAM, Grad-CAM++ and ODAM (ours). In the second questionnaire, the human is asked to choose the more reasonable heat map from the two explanations, which are generated from models of different performance (36.6% mAP and 42.3% mAP). The labels for options are assigned randomly for each question.

A.3 More Ablation Studies

A.3.1 Effects of thresholds in Odam-NMS

Figure 7 shows the results comparing various combinations of low and high correlation thresholds, T^l and T^h, for Odam-NMS with the FCOS detector. We compare with classical NMS, corresponding to $T^l = 0, T^h = 1$. The results for all the three metrics are improved by increasing T^l to 0.1-0.2, which indicates that some high-IoU crowded objects are successfully kept through their low correlation values. Then with the T^l further increasing, MR and JI starts to get worse, since more false positives are introduced. As for T^h, two proposals are regarded as the same object if their correlation exceeds T^h, even though their IoU is smaller than the T_{iou}. Since using $T^h < 1$ will reduce the recall rate, and AP_{50} is highly depends on the recall, T^h shows no benefit to AP_{50}. MR and JI have better performance by decreasing the T^h when T^l is fixed. This indicates that using a $T^h < 1$ can indeed remove low-IoU false positives, although the performance improvement is slight. Based on the results in Fig. 7, we adopt $T^h = 0.8$ and $T^l = 0.2$ in the experiments.

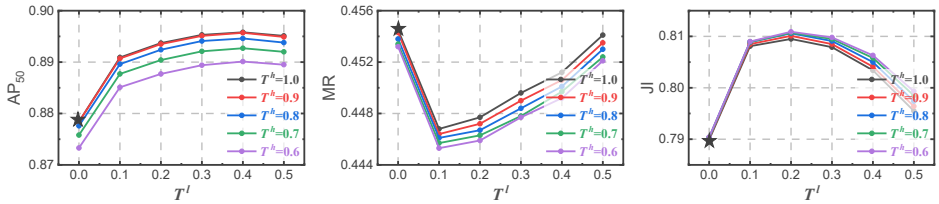

Figure 7: Effects of thresholds T^l and T^h in Odam-NMS. The black star marks the results for classical NMS, in which $T^l = 0$ and $T^h = 1$.

Table 6: Comparison of recalls on the "crowd" and "sparse" set from CrowdHuman validation set.

	Ground truth	FasterRCNN	FasterRCNN +ODAM-NMS	Δ	FCOS	FCOS +ODAM-NMS	Δ
Total	99,481	79,090 (79.5%)	**80,111 (80.5%)**	**+1%**	74,946 (75.3%)	**80,650 (81.1%)**	**+5.8%**
Sparse	78,273	65,480 (83.6%)	**65,639 (83.8%)**	**+0.2%**	61,890 (79.0%)	**64,726 (82.7%)**	**+3.7%**
Crowd	21,208	13,610 (64.2%)	**14,472 (68.2%)**	**+4%**	13,056 (61.6%)	**15,924 (75.1%)**	**+13.5%**

A.3.2 Analysis on recalls with Odam-NMS

To verify that more crowded objects can be recalled using Odam-NMS, we compare the recalls of the baseline detectors with or without Odam-NMS for both crowded and uncrowded instances. Since the recall is related to the confidence score threshold, we use the thresholds corresponding to the best JI for each method for fair comparison. Based on (Chu et al., 2020), we define the "crowd" set and "sparse" set, where the ground-truth boxes that overlap with some other ground truth with $IoU > 0.5$ comprise the "crowd" set and the other GT boxes as the "sparse" set. The results are shown in Tab. 6. The recall percentage on the crowd set is much lower than on the sparse set. Using Odam-NMS improves the recall percentage of crowded objects compared to the baseline, e.g., recall is improved by 4% for Faster R-CNN and 13.5% for FCOS.

A.3.3 Odam-NMS with and without Odam-Train

In Sec. 4.2, we evaluate Odam-NMS with the model when using Odam-Train. Here we provide the ablation studies evaluating Odam-NMS with and without using Odam-Train. The results are shown in the Tab. 7. When using the classical NMS, the baseline detector model yields similar and comparable results with and without using Odam-Train, which demonstrates that Odam-Train will have little influence on the baseline model performance when improving the explanation ability. This is a desirable property since we hope that providing explanations will not hinder the detector performance. As for Odam-NMS, Odam-Train brings an obvious improvement with the same parameter setting ($T^h = 0.8$ and $T_l = 0.2$) as compared to without Odam-Train. This shows that model can be trained to give more consistent and separated explanations that benefit duplicate detection removal. Furthermore, without Odam-Train, Odam-NMS needs the stricter judgment conditions to make more reasonable decisions, such as increasing T^h and reducing T_l, to obtain better results.

Table 8 illustrates the recalls on the "crowd" and "sparse" set when the FCOS model is trained with or without Odam-Train, and uses classical NMS or Odam-NMS in the post-processing. When using NMS with Odam-Train or Odam-NMS without Odam-Train, the recall rate is improved compared with the classical NMS without Odam-Train. However, the comprehensive metrics (e.g. AP, JI and MR) are not better accordingly (shown in Tab. 7) because the number of false positives is also

(a) trained model (b) untrained model

Figure 8: Sanity check. The predictions of "person" and corresponding heat maps generated from trained model and untrained model (with weight randomization).

Table 7: Comparisons of NMS performances with and without Odam-Train on the CrowdHuman validation set for both FCOS and Faster RCNN detectors. T^h and T^l are the correlation thresholds in the Algorithm 1. The IoU threshold for all NMS methods is 0.5.

	ODAM-Train	T^h	T^l	FCOS			Faster RCNN		
				AP↑	JI↑	MR↓	AP↑	JI↑	MR↓
NMS		-	-	87.8	78.4	45.5	86.9	79.5	43.2
	√	-	-	87.5	78.9	45.6	87.0	79.3	43.8
ODAM-NMS		0.8	0.2	87.5	78.5	54.0	88.9	78.7	44.3
		0.9	0.1	88.6	80.4	45.5	**89.0**	79.8	43.7
	√	0.8	0.2	**89.3**	**81.1**	**44.5**	88.1	**80.5**	**42.8**

Table 8: Comparison of recalls using NMS and ODAM-NMS for FCOS detector model with and without ODAM-Train on the "crowd" and "sparse" set from CrowdHuman validation set. "Conf." is the confidence threshold used to give the best JI score. For ODAM-NMS, the correlation thresholds T^h and T^l are set to 0.8 and 0.2.

	GT	NMS		ODAM-NMS	
ODAM-Train	-		√		√
Total	99,481	74,946 (75.3%)	78,097 (78.5%)	**80,697 (81.1%)**	80,650 (81.1%)
Sparse	78,273	61,890 (79.0%)	64,252 (82.1%)	**65,402 (83.6%)**	64,726 (82.7%)
Crowd	21,208	13,056 (61.6%)	13,845 (65.3%)	15,295 (72.1%)	**15,924 (75.1%)**

increased. Specifically, using Odam-NMS with Odam-Train, the recall is best on the crowd set and also obtains superior performance in Tab. 7 by reducing the number of false positives.

In summary, the ablation studies indicate that, since Odam-NMS makes decisions based on heat-map correlations, it relies on good quality explanations, and using Odam-Train is beneficial because it encourages the model to produce consistent and distinctive heat maps on detections of the same or different object.

A.4 More evaluations of visual explanations

Here we provide more evaluations about the visual explanations generated by ODAM.

A.4.1 Sanity checks

Adebayo et al. (2018b) develops sanity checks for saliency methods. Specifically, they compare explanation methods to edge detection techniques, and show that some methods are independent of both the model or training data, but still produce outputs visually similar to those of explanation methods. We adopt the model parameter randomization test proposed in (Adebayo et al., 2018b) to compare the predicted heat maps of the trained model and the untrained model. The Fig. 8 shows that the weight randomization results in totally incorrect predictions and corresponding heat maps, which means that our method is related to the predicted instances and relies on the model parameters to produce the explanations.

A.4.2 Analyzing error modes of detector

We use ODAM to analyze the error modes of detector. For the high confidence but poorly localized cases, we generate explanations of the wrong predicted extents and compare them with the correct localization results. As shown in Fig. 9, the model highlights that the wrong extents were misled by the leg of the person and the sea horizon.

To analyze classification decisions of the model, we generate explanations of the class scores. In Fig. 10, when focusing on both the monitor and keyboard, the model correctly classifies the instance as "laptop", while a fractional attention (only on the keyboard itself) results in predicting class "keyboard". Thus we may infer that the model requires seeing the laptop screen to predict "laptop". However note that the laptop keyboard has unique features (e.g., the trackpad) compared to a normal keyboard. Thus, this may be a particular failure mode of the detector.

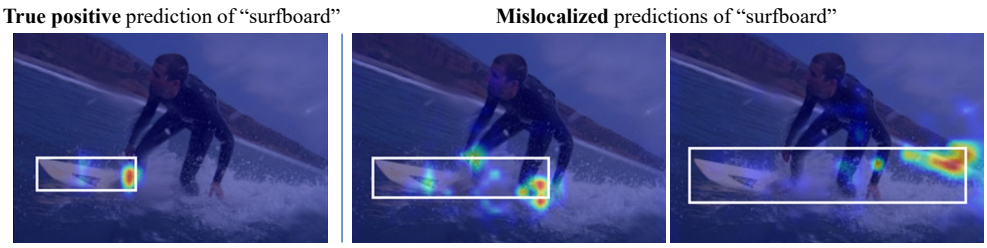

Figure 9: Explanations of the predictions of the right extent (x_2 in bounding boxes) for different predictions of "surfboard". The heat maps for the mislocalized predictions highlight the visual features that induced to the wrong extents (the leg on the right, and the sea horizon).

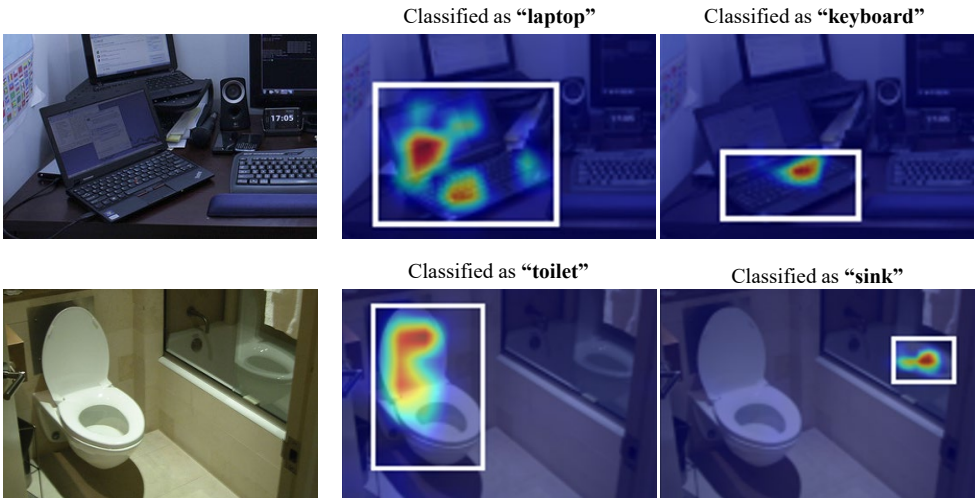

Figure 10: Explanations of the class scores of different predictions. In the first row, the model puts attention on only part of the laptop and predicts "keyboard". In the second row, the model focuses only on the toilet bowl and misclassifies the object as "sink".

The second row of Fig. 10 shows that the model correctly predicts the "toilet" class using the lid of the toilet. However, the model predicts "sink" on the toilet's reflection in the glass because it can only see the toilet bowl, and the lid is partially obscured. Again this shows a particular failure mode of the detector, where it relies too much on the toilet lid to predict the "toilet" class.

A.4.3 More comparisons of different explanation methods

We provide more comparisons of heat maps from D-RISE, Grad-CAM, Grad-CAM++, and our ODAM in Fig. 11.

A.4.4 More visualizations of each detection attribute

We provide more visualized explanations by ODAM for some high-confidence true positive predictions of the baseline FCOS detector in Fig. 12. The heat maps for the class scores and four regression values are displayed in each column.

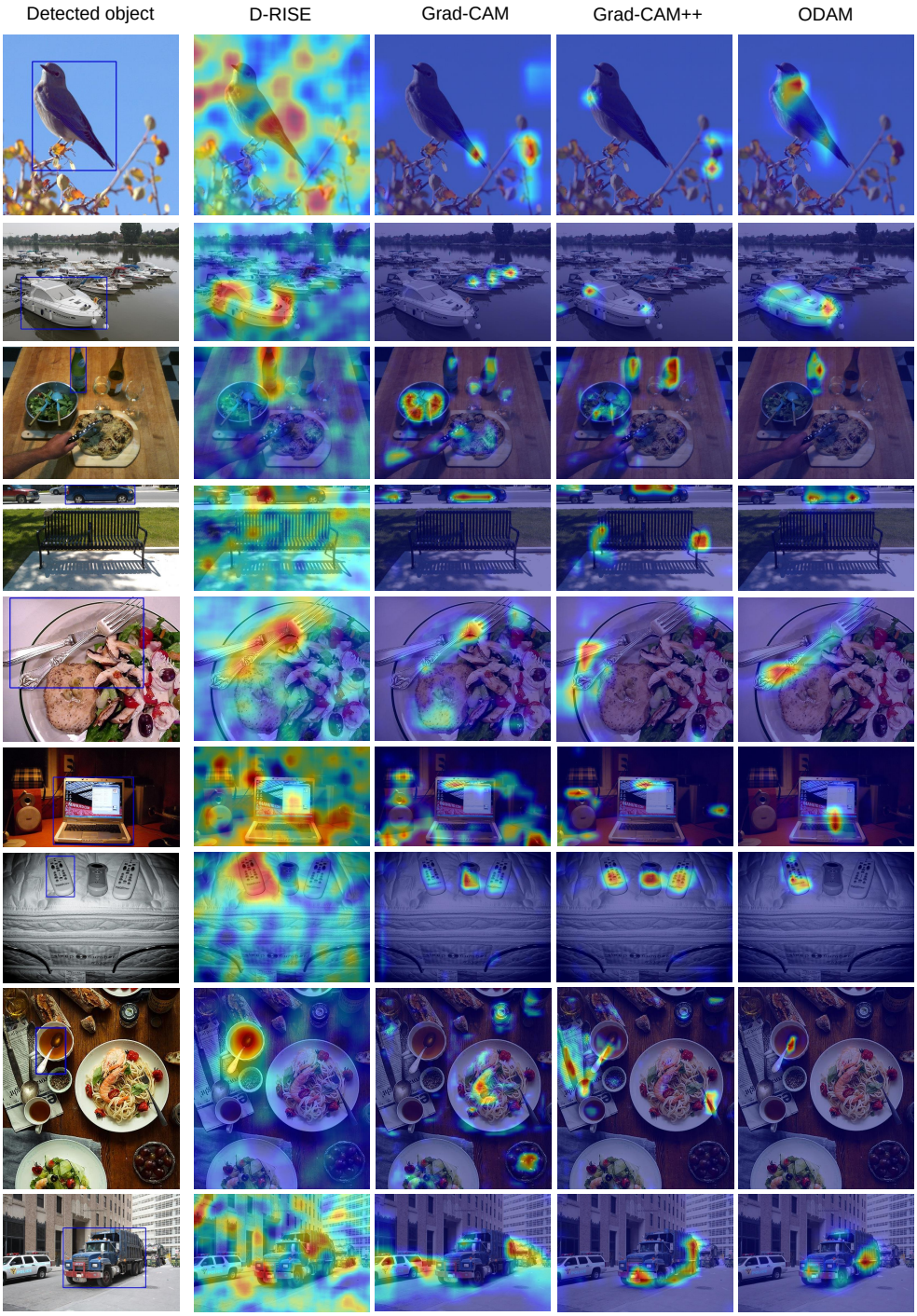

Figure 11: Visual comparison of our approach with other approaches on explaining object detection. The blue bounding box shows the explained detected object.

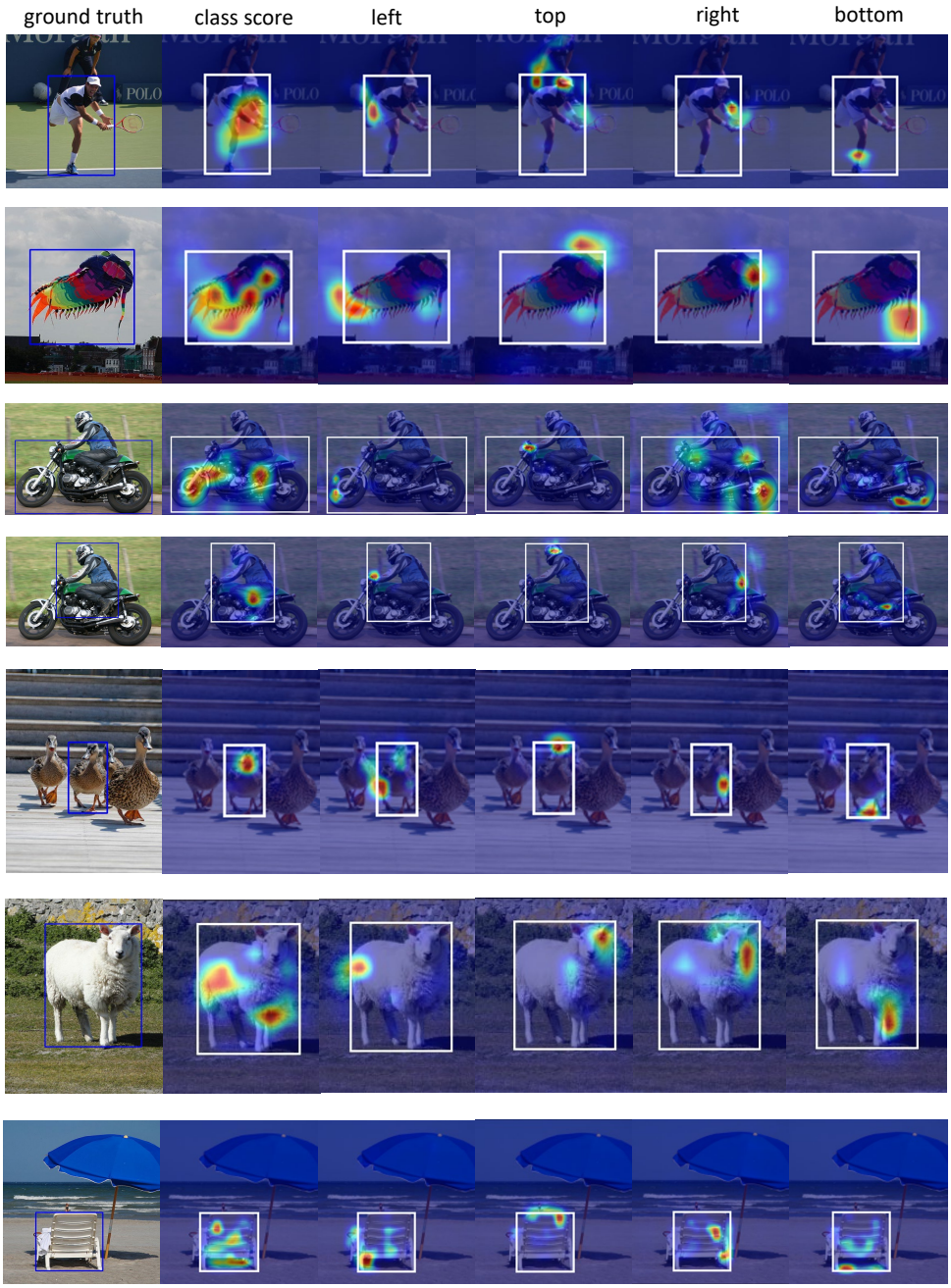

Figure 12: Visualized explanations of the class score and the regression of left, top, right, and bottom extents, respectively.